INTERNATIONAL JOURNAL FOR NUMERICAL METHODS IN FLUIDS
Int. J. Numer. Meth. Fluids **29**: 685–703 (1999)

FULLY NON-LINEAR FREE-SURFACE SIMULATIONS BY A 3D VISCOUS NUMERICAL WAVE TANK

JONG-CHUN PARK[a], MOO-HYUN KIM[a,*] AND HIDEAKI MIYATA[b]

[a] *Department of Civil Engineering, Texas A&M University, College Station, TX, USA*
[b] *Department of Naval Architecture and Ocean Engineering, University of Tokyo, Tokyo, Japan*

SUMMARY

A finite difference scheme using a modified marker-and-cell (MAC) method is applied to investigate the characteristics of non-linear wave motions and their interactions with a stationary three-dimensional body inside a numerical wave tank (NWT). The Navier–Stokes (NS) equation is solved for two fluid layers, and the boundary values are updated at each time step by a finite difference time marching scheme in the frame of a rectangular co-ordinate system. The viscous stresses and surface tension are neglected in the dynamic free-surface condition, and the fully non-linear kinematic free-surface condition is satisfied by the density function method developed for two fluid layers. The incident waves are generated from the inflow boundary by prescribing a velocity profile resembling flexible flap wavemaker motions, and the outgoing waves are numerically dissipated inside an artificial damping zone located at the end of the tank. The present NS–MAC NWT simulations for a vertical truncated circular cylinder inside a rectangular wave tank are compared with the experimental results of Mercier and Niedzwecki, an independently developed potential-based fully non-linear NWT, and the second-order diffraction computation. Copyright © 1999 John Wiley & Sons, Ltd.

KEY WORDS: numerical wave tank; finite difference method; fully non-linear free-surface condition; Navier–Stokes equation; density function; two-layer flow; vertical truncated cylinder; higher harmonic forces

1. INTRODUCTION

The interactions of large-amplitude waves with fixed or floating bodies are of fundamental interest to free-surface hydrodynamics and of immediate practical importance to naval architecture and ocean engineering. Over the past decade, a number of numerical wave tanks (NWT) have been developed to reproduce the main scientific features and non-linear effects observed in physical wave basins. This development has been made possible by the continuous increase in computer power. However, the fully non-linear free-surface computations are still computationally very intensive and require further development in methodology and algorithm.

In solving the fully non-linear waves and wave-body interactions, many researchers have used various potential-based boundary element methods (BEM). For instance, 2D problems

---

* Correspondence to: Department of Civil Engineering, Texas A&M University, College Station, TX, USA.

Contract/grant sponsor: OTRC/NSFI-ERC Program; Contract/grant number: #8721512
Contract/grant sponsor: NSFI-ERC Connectivity Award; Contract/grant number: #9720427
Contract/grant sponsor: Texas Advanced Research Program

CCC 0271–2091/99/060685–21$17.50

Received August 1997
Revised May 1998

have been investigated by Longuet-Higgins and Cokelet [1] and Clement [2] and 3D problems by Beck [3] and Dommermuth and Yue [4]. The boundary surface is discretized by a number of surface elements and the velocity potential (or source strength) on each element is solved by the Fredholm-type integral equation that can be converted to a linear simultaneous algebraic equation with a full influence coefficient matrix. In this approach, only the boundary surface needs to be discretized, instead of the entire fluid volume.

On the other hand, several authors tackled the NWT simulations by the volume discretization method. For instance, Wu and Eatock-Taylor [5] used a potential-based finite element method (FEM), while Chen *et al.* [6] and Miyata and Park [7] developed finite difference methods (FDM) to solve the Navier–Stokes (NS) equation with fully non-linear free-surface conditions. For volume discretization methods, the entire fluid volume needs to be discretized, and thus the generation of the grid system in general becomes more complicated than surface discretization methods. However, the left-hand-side matrix in the volume discretization method becomes narrowly banded, and thus it usually takes less time to solve the resulting matrix equation. In addition, when the NS equation is used, the effects of wakes and separated flows behind a blunt body can be accounted for. However, the tracing of the exact free-surface location may be less accurate than the boundary element method.

In this paper, a finite difference simulation method has been developed using the Navier–Stokes equation and a modified marker-and-cell (MAC) method for the non-linear interactions of steep waves with a three-dimensional body in a NWT. The viscous stresses and surface tension are neglected in the dynamic free-surface condition, and the kinematic free-surface condition is satisfied by the density function method devised for two fluid layers. The method can simulate wave overturning around a three-dimensional body and the simulation can be continued even after wave breaking. The incident waves are generated by prescribing flexible flap-wavemaker motions at the inflow boundary, and the outflow waves are numerically dissipated inside an artificial damping zone located at the end of the tank.

The development and verification of the basic algorithms and computer programs has been published as a TUMMAC [7–11] series. The algorithm has been further refined and tested recently, and the computer program is used to investigate the fully non-linear interactions of steep waves with a truncated vertical cylinder. The computed results are extensively compared with the experiment of Mercier and Niedzwecki [12], conducted at the OTRC wave basin at Texas A&M University. The NS–MAC NWT simulations are also compared with an independently developed potential-based fully non-linear NWT program for cross-checking and identifying viscous effects. The fully non-linear NWT computations are also compared with the second-order diffraction computations to observe the performance of the potential-based perturbation theory. It is observed that the NS–MAC NWT can reliably predict the non-linear free-surface elevation, local pressure and wave forces, including a spectrum of higher harmonic components.

2. MARKER-AND-CELL FINITE DIFFERENCE METHOD

2.1. Governing equations and non-linear free-surface conditions

Assuming that the fluid consists of two layers and each fluid layer is incompressible and homogeneous, the governing equations are given by the following Navier–Stokes equations and continuity equations:

$$\frac{\partial \boldsymbol{u}}{\partial t} = -\frac{\nabla p}{\rho^{\langle k \rangle}} + \boldsymbol{a}^{\langle k \rangle}, \tag{1}$$

$$\rho^{\langle k \rangle} \nabla \cdot \boldsymbol{u} = 0, \tag{2}$$

where $k = 1, 2$ and

$$\boldsymbol{a} = -(\boldsymbol{u} \cdot \nabla)\boldsymbol{u} + \nu \nabla^2 \boldsymbol{u} + \boldsymbol{f}. \tag{3}$$

In the above equations, $\boldsymbol{u} = (u, v, w)$ is the velocity vector, p is the pressure, t is the time, ∇ is the gradient operator, ν is the kinematic viscosity, $\boldsymbol{f}$ is the external force including the gravitational acceleration, and the superscripts $\langle 1 \rangle$ and $\langle 2 \rangle$ denote the fluid below and above the interface (water and air in the present study) respectively. The density ρ is assumed to be constant in each fluid region.

In the time marching procedure, the solutions of the governing equations in each region are obtained separately at each time step. The configuration of the interface is determined by applying the fully non-linear free-surface condition. At the free surface S_{f} (see Figure 1), the following fully non-linear kinematic and dynamic conditions can be applied neglecting the viscous stress and surface tension:

$$\frac{\mathrm{D}(\eta - z)}{\mathrm{D}t} = 0 \quad \text{on } S_{\mathrm{f}}, \tag{4}$$

$$p^{\langle 1 \rangle} = p^{\langle 2 \rangle} \quad \text{on } S_{\mathrm{f}}, \tag{5}$$

where η denotes the free-surface profile (wave height function), D is the total derivative, and z represents the vertical co-ordinate. Equation (4) means that the particle on the free-surface moves with the free-surface. The condition cannot be used for strongly interacting free-surface motions, such as overturning or broken waves. To overcome this limitation, the following density function equation is used in the present method instead of Equation (4):

$$\frac{\partial M_\rho}{\partial t} + u\frac{\partial M_\rho}{\partial x} + v\frac{\partial M_\rho}{\partial y} + w\frac{\partial M_\rho}{\partial z} = 0, \tag{6}$$

where the marker-density function M_ρ takes the value between $\rho^{\langle 1 \rangle}$ and $\rho^{\langle 2 \rangle}$ all over the computational domain, and this scalar value has the meaning of porosity in each cell. In case of air–water flow, this value denotes the volume fraction of water in a cell. Equation (6) is

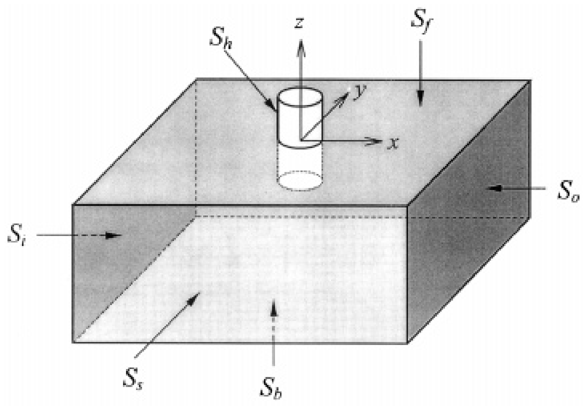

Figure 1. Co-ordinate system and computational domain.

calculated at each time step and the free-surface location is determined to be a point where the density function takes the mean value of $\rho^{\langle 1\rangle}$ and $\rho^{\langle 2\rangle}$ as

$$\bar{M}_\rho = \frac{\rho^{\langle 1\rangle} + \rho^{\langle 2\rangle}}{2}. \tag{7}$$

The interface location $\bar{M}_\rho$ is the same as the wave height function η in Equation (4), unless overturning and breaking waves are considered. Thus, Equation (6) is more general and solved for the movement of the fluid interface. After determining the free-surface location, the two fluid regions are treated separately and the governing equations (1) are integrated with the respective density, $\rho^{\langle 1\rangle}$ or $\rho^{\langle 2\rangle}$.

2.2. Algorithm and differencing scheme

The substantial part of the solution algorithm for each layer is similar to the previous TUMMAC method [7–11] in which the velocity and pressure points are defined in a staggered manner in a rectangular co-ordinate system. The computational procedure is shown in Figure 2. In the time marching process, the density function distribution is calculated from Equation (6) and the velocity field is updated through the Navier–Stokes equation (1). The boundary values of the velocities are then set on the new location of the interface. The new pressure field is determined by iteratively solving the following Poisson equation in each layer using the Richardson method:

$$\nabla \cdot \nabla P = \nabla \cdot \left(\boldsymbol{a} + \frac{\boldsymbol{u}^{(n)}}{\Delta t} \right) = \nabla \cdot \boldsymbol{b}, \tag{8}$$

$$P^{m+1} = P^m + \bar{\omega}(\nabla \cdot \nabla P - \nabla \cdot \boldsymbol{b}), \tag{9}$$

where $P = p/\rho$, and $\bar{\omega}$ is the relaxation factor set at a value smaller than unity. The superscript n denotes the time level and m the iteration level. The $\boldsymbol{b}$ term, which includes both diffusion and convection terms, is called the source term. The NS equations (1) are hyperbolic equations to be solved as an initial value problem, while the Poisson equation (8) is an elliptic equation to be solved as a boundary value problem. Equations (1) are solved by time marching and at every time step Equation (8) is solved by an iterative procedure. The cycle is repeated until the number of time steps reaches the predetermined value.

The finite difference scheme for the convective terms must be carefully chosen, since it often renders decisive influences on the results. In the present time simulation, a third-order upwind scheme with variable mesh size [10] is employed so that a variable mesh system can be used for all three directions. Writing a differencing scheme D as

$$D = \sum_{\imath=-2}^{2} c_\imath I^\imath, \tag{10}$$

where $c_\imath$ is the coefficient corresponding to the cell spacing and $I^\imath$ is the shifting operator defined as

$$I^\imath f(x) = f(x + \imath\Delta), \tag{11}$$

with Δ being the spacing, the coefficients $c_\imath$, of the third-order upwind differencing scheme in the x-direction, for instance, can be obtained from the following simultaneous equation:

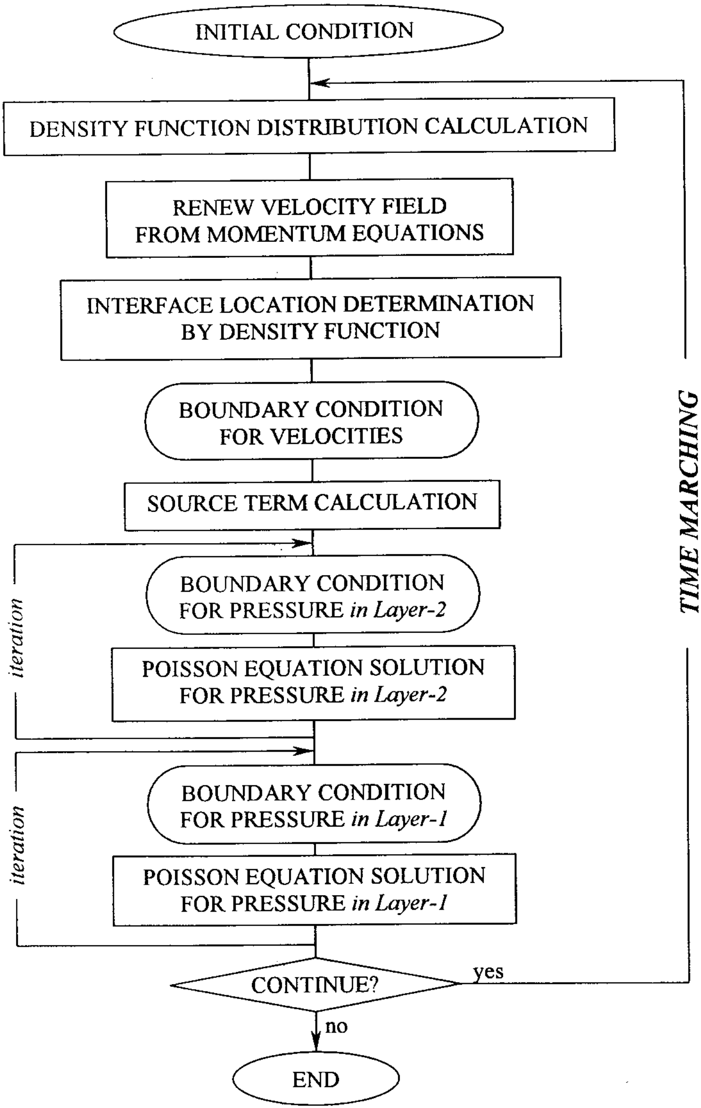

Figure 2. Flow chart of time marching scheme.

$$\begin{bmatrix} 1 & 1 & 1 & 1 \\ (\Delta x_0+\Delta x_1) & \Delta x_0 & \Delta x_{-1} & (\Delta x_{-1}+\Delta x_{-2}) \\ (\Delta x_0+\Delta x_1)^2 & \Delta x_0^2 & \Delta x_{-1}^2 & (\Delta x_{-1}+\Delta x_{-2})^2 \\ (\Delta x_0+\Delta x_1)^3 & \Delta x_0^3 & \Delta x_{-1}^3 & (\Delta x_{-1}+\Delta x_{-2})^3 \end{bmatrix} \begin{bmatrix} c_2 \\ c_1 \\ c_{-1} \\ c_{-2} \end{bmatrix} = \begin{bmatrix} -c_0 \\ 1 \\ 0 \\ 0 \end{bmatrix}, \tag{12}$$

in which Δx is the spacing in the x-direction. When c_0 is determined, the other coefficients can subsequently be obtained by solving Equation (12). When $\Delta x = \Delta$(constant), and $c_0 = 3/(2\Delta)$, the Kawamura's scheme is obtained. Similarly, setting $c_0 = 1/(2\Delta)$, the Agarwal's scheme is obtained. In the present study, $c_0 = 3/(2\Delta x_0)$ is used. Then, the advective term can be written as

$$u\frac{\partial}{\partial x} = \begin{cases} u_{i,j,k} \sum_{\iota=-2}^{2} c_\iota I^\iota & (\text{if } u_{i,j,k} \geq 0) \\ -u_{i,j,k} \sum_{\iota=-2}^{2} c_{-i} I^\iota & (\text{if } u_{i,j,k} < 0) \end{cases}. \tag{13}$$

On the other hand, a second-order-centered scheme is employed for the diffusive terms.

For the finite difference approximation of the density function equation (6), the second-order Adams–Bashforth method is used for the time differencing as follows:

$$M_\rho^{(n+1)} = M_\rho^{(n)} - \Delta t\left[\frac{3\hat{M}_\rho^{(n)} - \hat{M}_\rho^{(n-1)}}{2}\right], \tag{14}$$

where

$$\hat{M}_\rho = u\frac{\partial M_\rho}{\partial x} + v\frac{\partial M_\rho}{\partial t} + w\frac{\partial M_\rho}{\partial z}. \tag{15}$$

For the space differencing of Equation (6), the flux split method, which is like the third-order upwind differencing scheme, is used. The scheme can be written as follows for the first term for simplicity

$$\hat{M}_{\rho i} = u_0\left[\frac{M_{\rho i+1/2} - M_{\rho i-1/2}}{\Delta_i}\right], \tag{16}$$

where

$$M_{\rho i+1/2} = \begin{cases} M^{\mathrm{L}}_{\rho i+1/2} & (\text{if } u_{i+1/2} \geq 0) \\ M^{\mathrm{R}}_{\rho i+1/2} & (\text{if } u_{i+1/2} < 0)\text{'} \end{cases} \tag{17}$$

$$u_0 = \frac{u_{i-1/2} + u_{i+1/2}}{2}. \tag{18}$$

In the case of the variable mesh system, the values of $M^{\mathrm{L}}_{\rho i+1/2}$ and $M^{\mathrm{R}}_{\rho i+1/2}$ are determined following Sawada and Takahashi [14] as

$$\begin{aligned} M^{\mathrm{L}}_{\rho i+1/2} &= M_{\rho i} + \Delta_{\mathrm{L}1}(M_{\rho i} - M_{\rho i-1}) + \Delta_{\mathrm{L}2}(M_{\rho i+1} - M_{\rho i}) \\ M^{\mathrm{R}}_{\rho i+1/2} &= M_{\rho i} + (1 - \Delta_{\mathrm{R}1})(M_{\rho i+1} - M_{\rho i}) - \Delta_{\mathrm{R}2}(M_{\rho i+2} - M_{\rho i+1}) \end{aligned} \tag{19}$$

$$\begin{aligned} \Delta_{\mathrm{L}1} &= \frac{\Delta_i\Delta_{i+1}}{(\Delta_{i-1} + \Delta_i + \Delta_{i+1})(\Delta_{i-1} + \Delta_i)} \\ \Delta_{\mathrm{L}2} &= \frac{\Delta_i(\Delta_{i-1} + \Delta_i)}{(\Delta_{i-1} + \Delta_i + \Delta_{i+1})(\Delta_i + \Delta_{i+1})} \\ \Delta_{\mathrm{R}1} &= \frac{\Delta_{i+1}(\Delta_{i+1} + \Delta_{i+2})}{(\Delta_i + \Delta_{i+1} + \Delta_{i+2})(\Delta_i + \Delta_{i+1})} \\ \Delta_{\mathrm{R}2} &= \frac{\Delta_i\Delta_{i+1}}{(\Delta_i + \Delta_{i+1} + \Delta_{i+2})(\Delta_{i+1} + \Delta_{i+2})} \end{aligned} \tag{20}$$

The dynamic free-surface condition of Equation (5) is implemented by the so-called ‘irregular star’ technique [15] in the solution process of the Poisson equation for the pressure.

In the present problem, it is very important to extrapolate the physical values into the other layer, since the fluid motions at the interface are determined by the interaction between the two fluids. Therefore, the pressure at the interface is determined by extrapolating the pressure of the fluid $\langle 2 \rangle$ to the interface location. The pressures are extrapolated with zero gradient in the approximately normal direction to the free-surface, while the static pressure difference in the vertical direction due to the gravity is taken into consideration. Similarly, the velocities are extrapolated at the interface with approximately no normal gradient from fluid $\langle 1 \rangle$ to fluid $\langle 2 \rangle$, i.e. the velocities u_{fs} on the free-surface are extrapolated as follows:

$$u_{f\mathrm{s}} = \frac{\sum_k \left(\dfrac{u_k}{\ell_k} \right)}{\sum_k \left(\dfrac{1}{\ell_k} \right)}, \tag{21}$$

where k is the number of velocities used for the extrapolation, u_k the velocities in layer $\langle 1 \rangle$, and ℓ_k the length between the location of the velocity u_k and the free-surface. This treatment grossly accords with the viscous tangential condition at the free-surface [13].

2.3. Other boundary conditions

A no-slip body boundary condition is imposed on the body surface S_{h} (see Figure 1). Since the Cartesian grid system is used for the flow around a three-dimensional body of complex geometry, a special treatment of a porosity function is employed on the body surface, as detailed in Miyata and Yamada [11]. The local surface of the body is represented by the porosity that indicates the rigid portion of the boundary cell and by the unit vector normal to the body surface.

At the inflow boundary of the three-dimensional rectangular computational domain $\langle 1 \rangle$, a numerical wavemaker is established by prescribing the inflow velocities based on the water particle velocities of the linear wave (or Stokes second-order wave), which is like a flexible flap wavemaker. The inflow velocities in the region $\langle 2 \rangle$ are set to be zero. The pressure and the values of density function are extrapolated with no-normal gradient condition in the horizontal direction.

The side-wall boundary is assumed to be a free-slip rigid wall as

$$\left. \frac{\partial \Xi}{\partial n} \right|_{i,\mathrm{wall},k} = 0, \qquad v_{i,\mathrm{wall},k} = 0, \quad \text{on } S_{\mathrm{s}}, \tag{22}$$

where Ξ represents the velocity components, the pressure, or the values of marker-density and n means the normal direction.

At the top and bottom boundaries of the computational domain, no-normal gradient boundary conditions are given for the velocity and the hydrostatic pressure is given assuming that the vertical distances from the interface are sufficiently large in comparison with the wave height of interest, i.e.

$$\left. \frac{\partial \Xi}{\partial n} \right|_{i,j,\mathrm{wall}} = 0, \qquad p_{i,j,\mathrm{wall}} = p_{\mathrm{static}}, \quad \text{on } S_{\mathrm{t}} \cup S_{\mathrm{b}}, \tag{23}$$

where p_{static} is the static pressure at the top or bottom surface. In case the water depth is not large enough, the free-slip condition for the velocity and zero-normal gradient condition for the pressure are used as bottom boundary conditions, while the pressure at the inflow boundary is given by the static pressure.

One of the most critical issues for fully non-linear NWT simulations is the numerical implementation of a robust downstream open boundary condition. A well-designed open boundary condition is particularly important to reduce the size of the computational domain. In the present study, an artificial damping scheme [9] is employed in the added dissipation zone to dissipate all the wave energy of outgoing waves. The artificial damping added to the right-hand-side of Equation (3) can be expressed as follows:

$$\left\{0.0,\ 0.0,\ \alpha\left(\frac{x-x_s}{x_e-x_s}\right)^2\left(\frac{z_b-z}{z_b-z_{fs}}\right)\right\}\cdot \boldsymbol{u}:\quad \text{in layer } \langle 1\rangle,\quad x_s<x<x_e \quad\text{and}\quad z_b<z<z_{fs}; \tag{24a}$$

$$\left\{0.0,\ 0.0,\ \alpha\left(\frac{x-x_s}{x_e-x_s}\right)^2\left(\frac{z-z_t}{z_{fs}-z_t}\right)\right\}\cdot \boldsymbol{u}:\ \text{in layer } \langle 2\rangle,\quad x_s<x<x_e \quad\text{and}\quad z_{fs}<z<z_t; \tag{24b}$$

in which the control parameter $\alpha = -0.5$ is used. The subscripts s and e denote the start and end points of the added dissipation zone in the x-direction and b, fs and t denote the bottom, free-surface and top positions of the damping zone in the z-direction respectively. In the damping zone, the mesh size is gradually increased in the horizontal direction to provide additional numerical damping.

3. COMPUTATIONAL RESULTS AND DISCUSSIONS

To demonstrate the usefulness and accuracy of the NS–MAC NWT, results are presented here for two different applications of interest; (i) non-linear propagation of regular waves generated by prescribing an inflow velocity similar to a flexible flap wavemaker, and (ii) non-linear diffraction by a truncated vertical cylinder inside a rectangular wave tank with side-walls, for which the experimental results of Mercier and Niedzwecki [12] are available. To obtain steady state results, a large number of periods need to be simulated, which is also a particularly useful test to assess the overall stability and the effectiveness of the numerical open boundary condition. The computational results for the truncated cylinder are also compared with an independently developed potential-based fully non-linear NWT program (Celebi *et al.* [16,17] and Kim *et al.* [18]) and the second-order diffraction computation (Kim and Yue [19]).

3.1. Numerical tests for the inflow and outflow boundaries

The incoming non-linear waves are generated by the prescribed motion of a flexible flap wavemaker, which is given by the fluid particle velocity of a linear wave of given height and period. Although the wavemaker motion follows the linear particle velocity, the essential non-linear features are to be present because the generated waves immediately satisfy the fully non-linear free-surface condition. At the other end of the NWT, an artificial damping zone is implemented to dissipate the energy of outgoing waves.

First, the generation, propagation and absorption of waves without obstruction are tested. The dimension of the NWT is described in Table I. A three-dimensional snapshot is shown in Figure 3. The waves remain long crested and are not affected by the presence of the side-walls. Next, the time histories of free-surface profiles at three different locations along the centerline of the tank are shown in Figure 4. The wave probes are located at $0.1L$, $1.0L$ and $2.0L$ ($L=$ wavelength) from the wavemaker and the wave period $T=1.0$ s and wave steepness $H/L=1/21$ are used. The wave trains rapidly reach a steady state and the profiles maintain uniform shapes after that. The wave profiles also exhibit typical non-linear features, such as higher and narrower crests and smaller and flatter troughs. To observe these non-linear

Table I. Condition of calculation

Truncated vertical cylinder (m)	
Radius r	0.23
Draft d	1.34
Computational domain	
Longitudinal (except for damping region)	$-10.4r \sim 8.7r$
Lateral	$0 \sim 12.2r$
Vertical	$-4.2d \sim 2.2d$
Waves	
Period T (s)	0.87, 1.00, 1.40 and 2.00
Steepness $\varepsilon = H/gT^2$	0.0075
Height $H = 2a$ (cm)	5.56, 7.35, 14.41 and 29.40
Grid spacing (cm)	
Longitudinal (except for damping region)	4
Lateral	4
Vertical (minimum)	$H/20$
Number of grids	$130 \times 70 \times 75$
Time increment Δt (s)	$T/2000$

features more clearly, the steady wave profile of one wave period is compared with those of Stokes first- and second-order waves, as shown in Figure 5. The present non-linear results are closer to the second-order wave theory than the first-order one. In Figure 6, a series of higher harmonics of the incident waves are obtained by fast Fourier transformation (FFT). It shows that a series of higher harmonics are present in the incident wave even if the wavemaker is driven by the linear velocity profile.

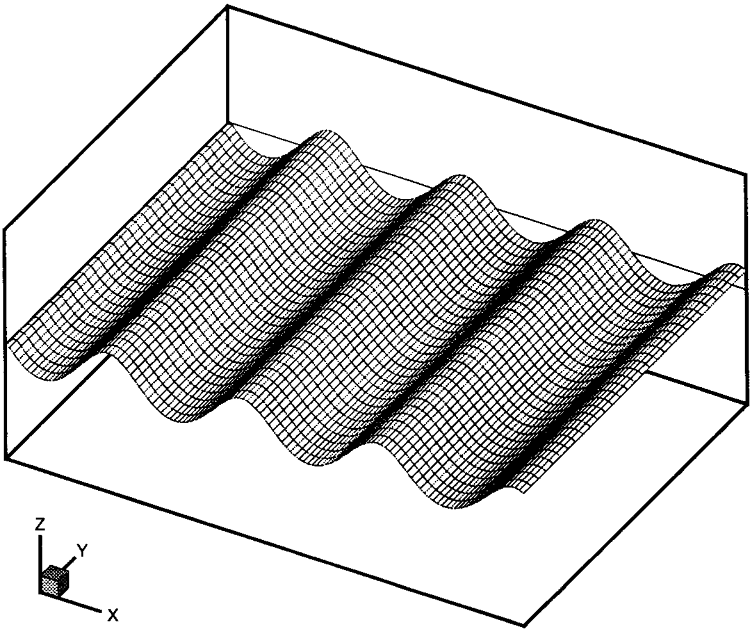

Figure 3. Schematic view of 3D NS–MAC numerical wave tank.

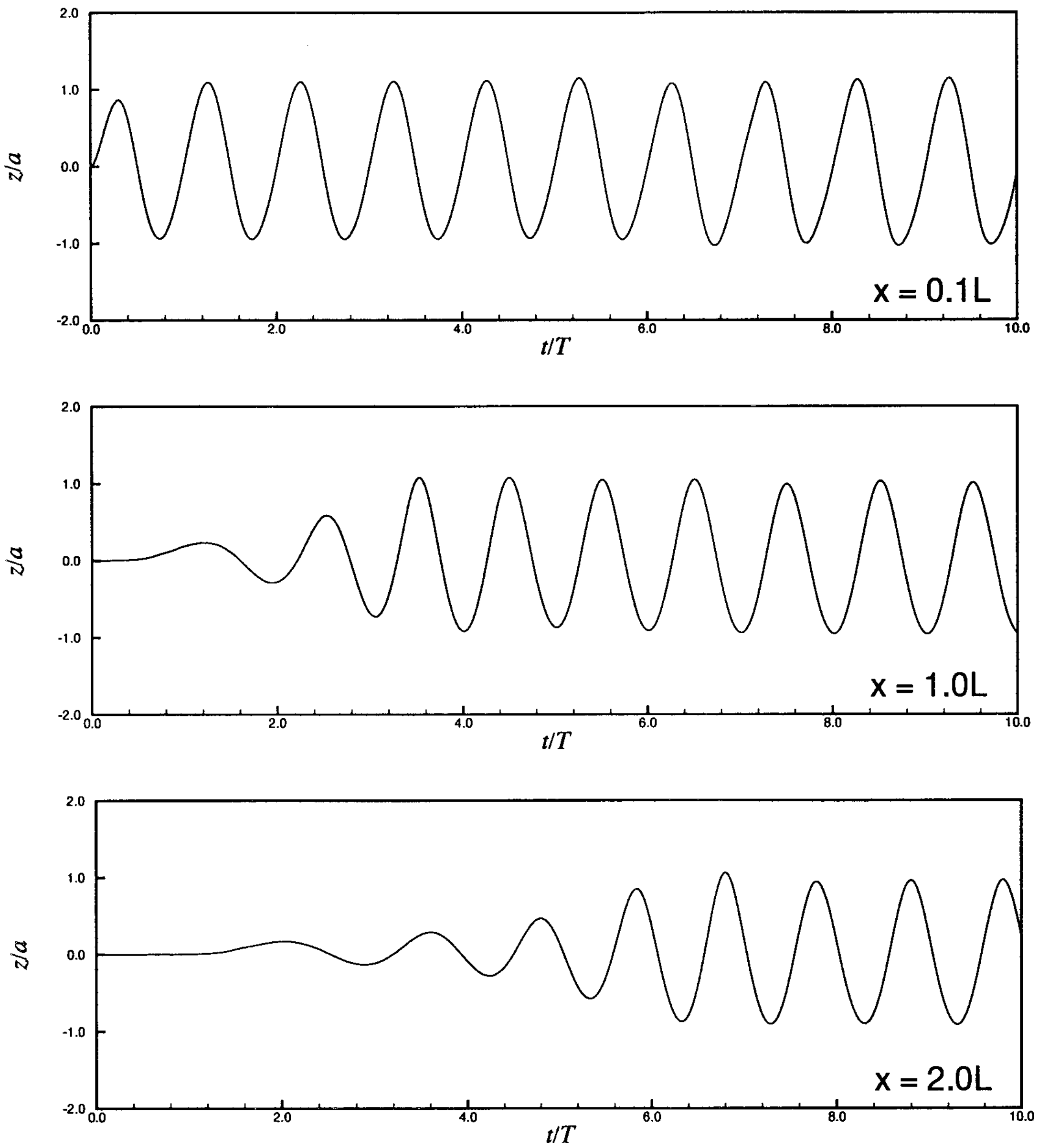

Figure 4. Free-surface time series at three locations; $x = 0.1L$, $1.0L$ and $2.0L$, where L is wavelength.

Next, to verify the robustness of the outflow boundary condition, two simulations are conducted for the same wave condition with two different lengths of the NWT, as shown in Figure 7. Here, the shorter region is made by the 25% reduction of the longer region. The agreement between the two wave profiles is very good, which implies that there is apparently no wave reflection from the artificial damping zone. The relative error between the two simulations is within 2% of the incident wave height.

3.2. *Non-linear waves around a vertical truncated cylinder*

In Figures 8–11, the viscous NWT simulations with a stationary vertical truncated cylinder (radius $r = 23$ cm, draft $d = 1.34$ m) are compared with the Mercier and Niedzwecki's [12] experiments conducted in the OTRC three-dimensional wave basin ($50 \times 33 \times 6$ m^3) located at Texas A&M University. The wave basin is equipped with a 48-segment hydraulically driven flap-type wavemaker. The conditions for the present computation are summarized in Table I. The cylinder is located about $10r$ away from the numerical wavemaker and the distance from the center of the cylinder to the side wall is about $12r$. The computations with four wave periods $T = 0.87$, 1.00, 1.40 and 2.00 s are performed while keeping the wave steepness $\varepsilon = H/gT^2 = 0.0075$ (or $H/L = 1/21$) constant for each case. The range of Reynolds number is about $9 \times 10^4 \sim 2 \times 10^5$ and the Keulegan–Carpenter (K–C) number $0.4 \sim 2$. The small K–C

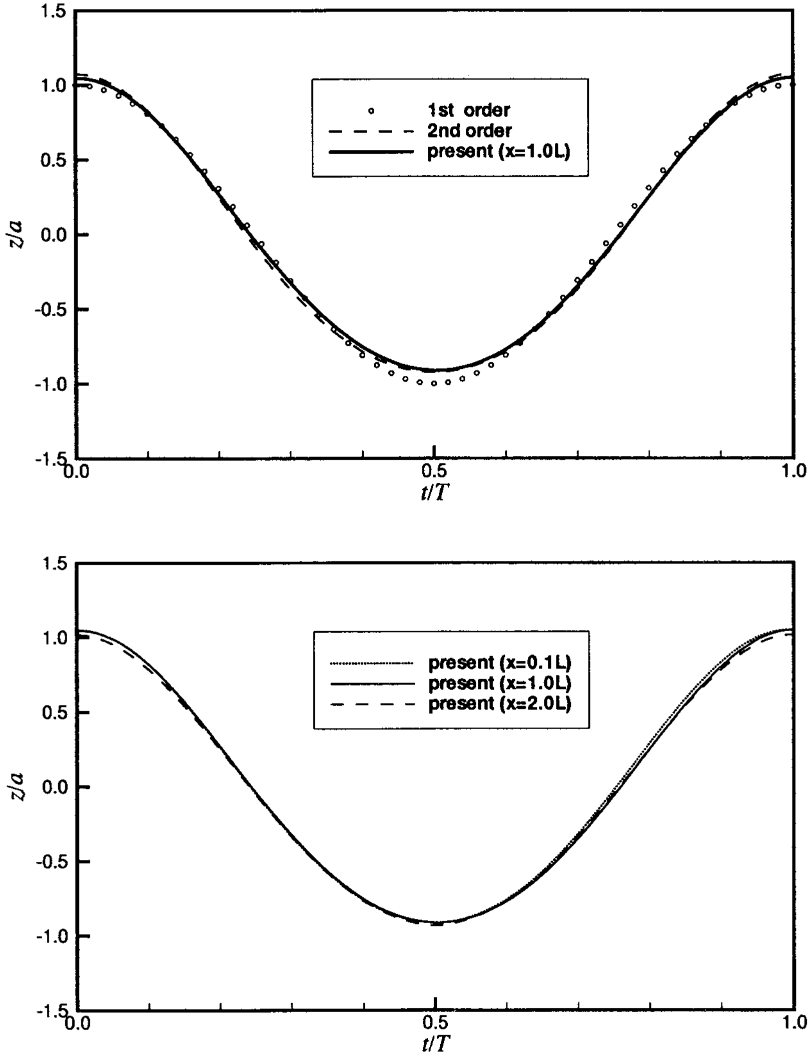

Figure 5. Top: comparison of first- and second-order Stokes waves with the fully non-linear incident waves generated by the NS–MAC NWT; bottom: free-surface profiles at three locations.

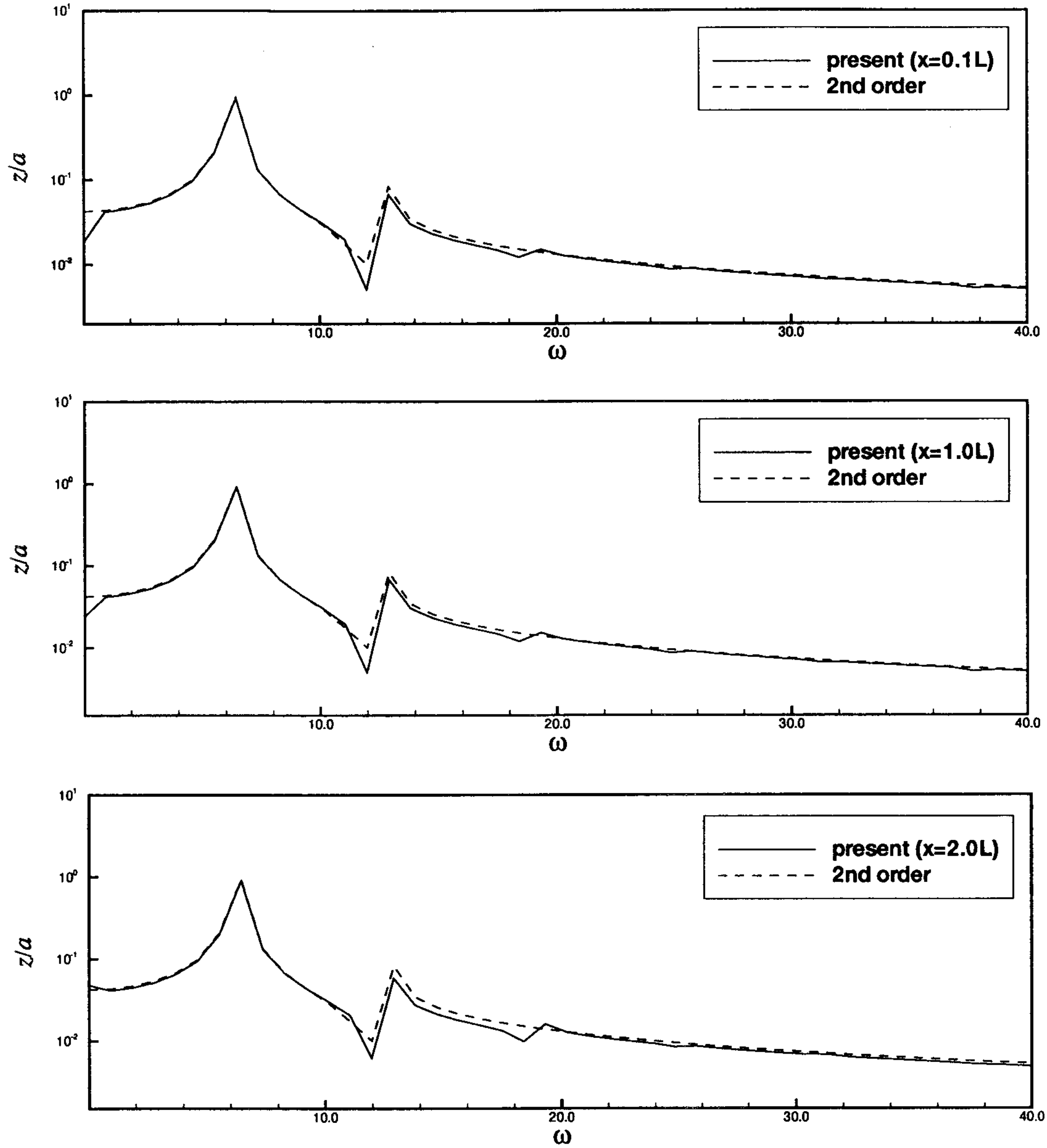

Figure 6. Comparison of the spectra of NWT incident waves with those of second-order Stokes waves at three different locations.

number indicates that inertia effects are more important than viscous effects. The same grid system (130 × 70 × 75) is used for all the cases presented here. In the longitudinal and lateral directions, an equal spacing is used except for the damping region. In the vertical direction, a variable mesh system (increasing size with depth) is employed and the minimum grid size is determined based on the incident wave height. The time increment used for this computation is $T/2000$ and the total number of grids in the half fluid domain is about 682500, including the damping zone. The damping zone is discretized by 20 × 70 × 75 cells. Using the third-order

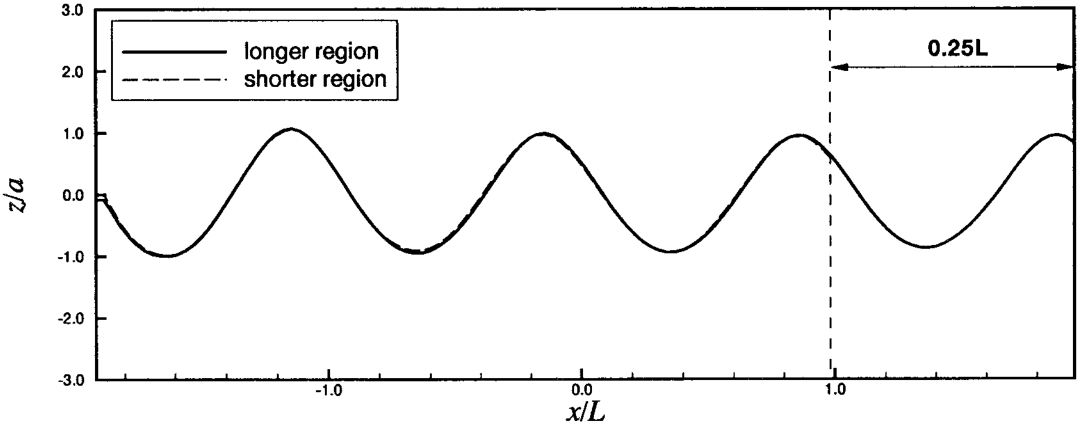

Figure 7. NWT simulations by two computational domains of different length.

upwind differencing scheme for the convection terms and the second-order Adams–Bashforth method for time marching, the overall scheme is stable even with a coarse grid system. However, the mesh size and time step have to be small to achieve a desirable accuracy. More detailed analysis for the stability and convergence of the present algorithm is reported in Park *et al.* [8,9].

To quantitatively observe the contribution of higher harmonics, their magnitudes are calculated by a FFT algorithm. Figures 9–11 show the comparisons of the measured and predicted first-order, second-order and third-order free-surface elevations and wave run up at five different locations (see Figure 8). The figures also show the corresponding results computed from a fully non-linear potential-based desingularized boundary integral equation method (DBIEM) and a second-order diffraction code. The DBIEM NWT uses a source distribution outside the computational boundary and a mixed Eulerian and Lagrangian (MEL) time marching scheme to update the free-surface. It also uses an artificial damping on the downstream free-surface and a piston-type wavemaker at the inflow boundary. The details are given in Celebi *et al.* [17]. The second-order diffraction computation is based on a boundary element method using constant panels (Lee *et al.* [20]). The second-order results are taken from Mercier and Niedzwecki [12].

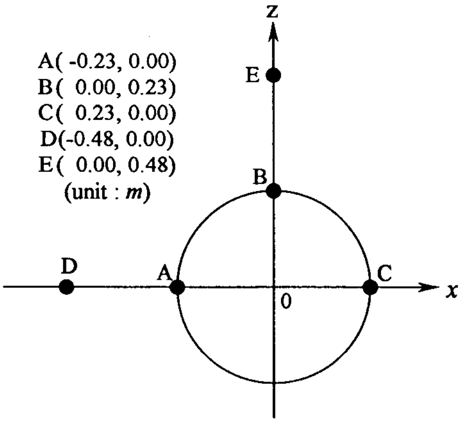

Figure 8. The location of wave probes for Figures 9–11.

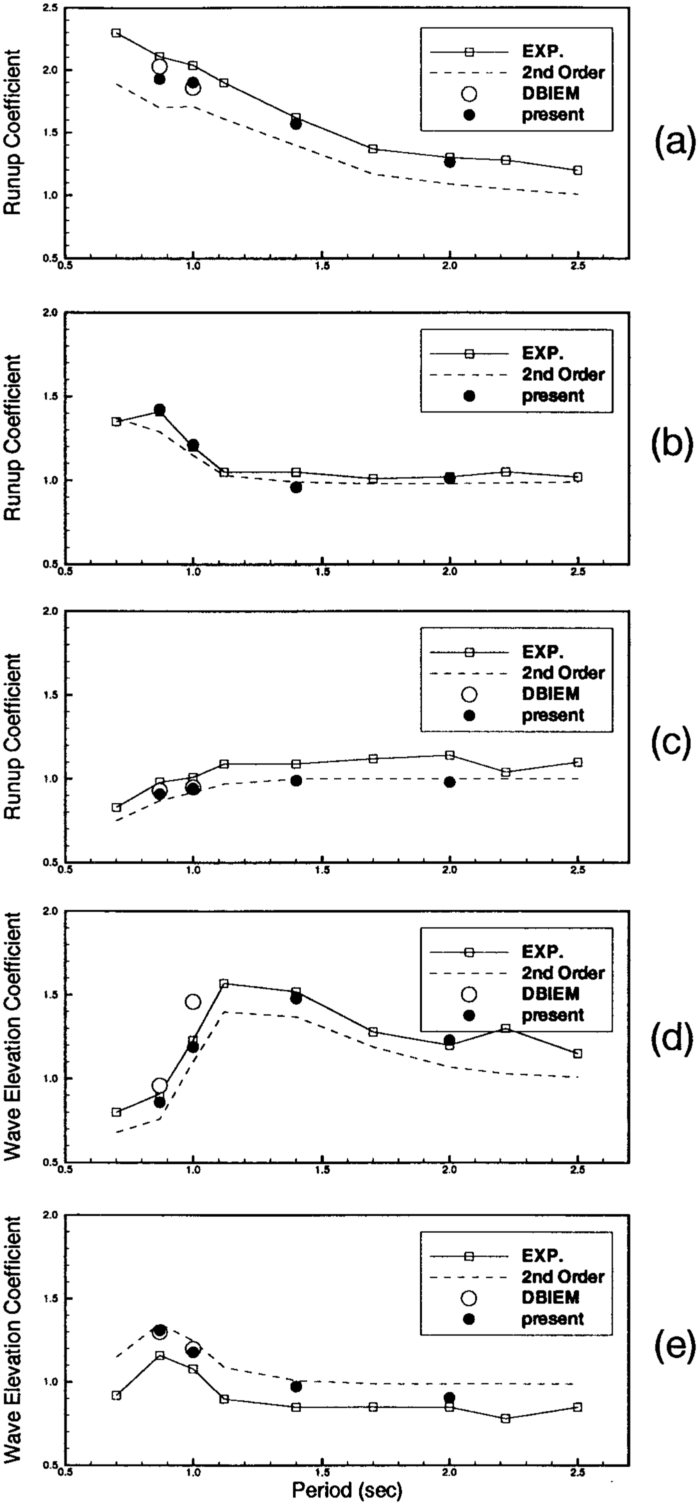

Figure 9. First-order wave run-up and elevation at five locations.

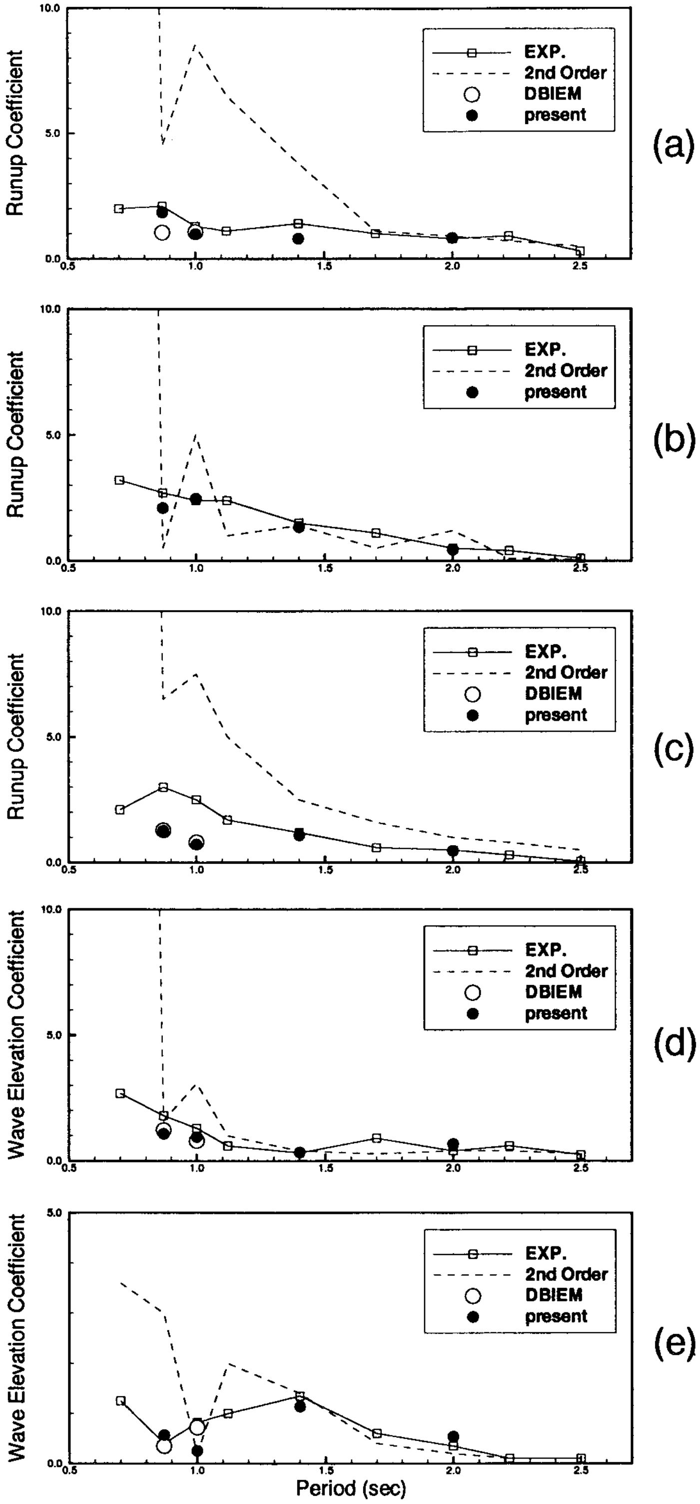

Figure 10. Second-order wave run-up and elevation at five locations.

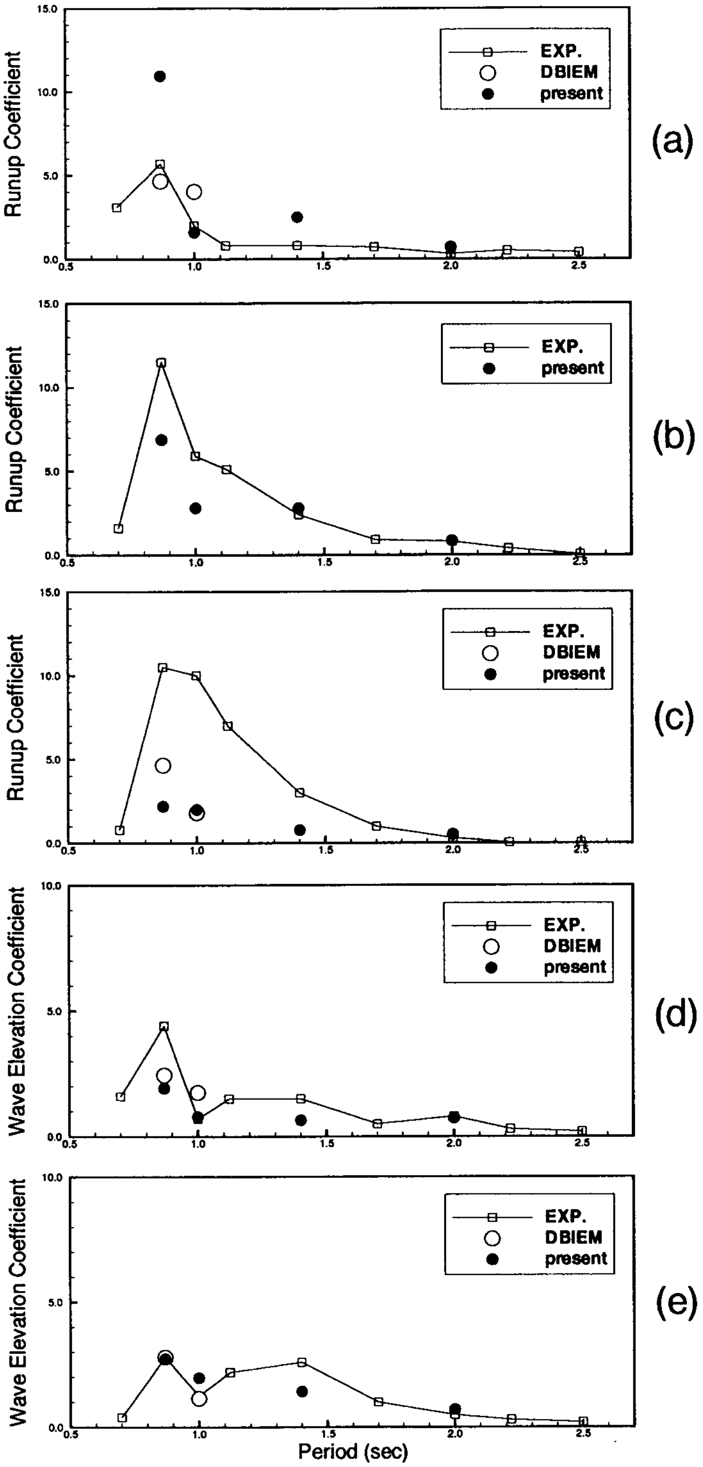

Figure 11. Third-order wave run-up and elevation at five locations.

Table II. Comparison of horizontal forces and pitch moments

	F_x			M_y		
	$F_x^{(1)}$	$F_x^{(2)}$	$F_x^{(3)}$	$M_y^{(1)}$	$M_y^{(2)}$	$M_y^{(3)}$
Second-order diffraction	5.88	0.50	—	10.18	2.09	—
DBIEM	5.93	1.28	3.64	10.51	3.02	7.75
NS–MAC	5.92	1.86	5.09	11.21	6.63	9.49

The first-harmonic results show that the simulations by NS–MAC NWT agree well with DBIEM simulations and correlate better with experiments than the second-order diffraction results. As for the second-harmonic components, the agreement between NS–MAC NWT simulations and measurements is still reasonable, while the results of the second-order diffraction computation tend to deviate a lot from the measured values, especially in short waves. Reasonable agreement is also seen for the third-harmonic components between the experimental values and the prediction by NWT simulations, except for the location C and the case of shortest wave. The discrepancy between the measured, NS–MAC NWT and DBIEM NWT results can be attributed to different wave generating mechanism and viscous effects. It is also mentioned in Mercier and Niedzwecki [12] that the wave amplitude for the shortest wave was too small and the resulting experimental data may not be reliable. At any rate, the overall agreement of the second- and third-order components between the measurements and NWT simulations is reasonably good despite the fact that the magnitudes of those higher harmonic components are very small. From these comparisons, it is seen that the fully non-linear simulations by the potential or viscous NWTs give more reliable results for the diffracted wave field around a three-dimensional body than the second-order diffraction theory.

Next, the horizontal forces and the pitch moments are compared with each other with respect to the center of the waterplane obtained by three different computational methods. The results are for $T = 1$ s. The forces and moments given in Table II are non-dimensionalized as follows:

$$F^{(1)} = \mathrm{Force}^{(1)}/\rho g r^2 a, \qquad F^{(2)} = \mathrm{Force}^{(2)}/\rho g r a^2,$$
$$F^{(3)} = \mathrm{Force}^{(3)}/\rho g a^3, \qquad M^{(1)} = \mathrm{Moment}^{(1)}/\rho g r^3 a,$$
$$M^{(2)} = \mathrm{Moment}^{(2)}/\rho g r^2 a^2, \quad M^{(3)} = \mathrm{Moment}^{(3)}/\rho g r a^3,$$

As for the first-order horizontal forces and pitch moments, the NWT simulations give slightly larger values than the second-order diffraction computation [19]. The second- and third-order components by the NS–MAC NWT tend to be greater than those by other

Table III. Hydrodynamic pressure at the bottom center

	NS–MAC NWT	Experiment	Second-order	DBIEM NWT
First-order	0.002	0.002	0.002	0.029
Second-order	0.13	0.17	0.12	0.21
Third-order	0.11	0.08	—	0.38

The pressures are non-dimensionalized by $p^{(1)}/\rho g a$, $p^{(2)} r/\rho g a^2$ and $p^{(3)} r^2/\rho g a^3$.

methods. The discrepancy may be attributed to the viscous effects around the cylinder and its bottom corner, and different run-up and incident waves.

Next, the predicted and measured hydrodynamic pressures at the bottom center of the cylinder are compared in Table III. It can be seen both in theory and experiment that higher harmonic pressure components more slowly attenuate with depth than the first-order pressure. As a result, the bottom pressure is dominated by higher harmonic components. This phenomenon may be related to the 'microseism' suggested by Longuet-Higgins [21]. The theoretical explanation of this phenomenon by using the second-order diffraction theory is given in Newman [22] and Kim and Yue [19].

Plate 1 shows two snapshots of the free-surface profiles around the vertical cylinder. The darker line on the cylinder represents the waterline. The bottom figure is the case when the wave crest hits the weather side of the cylinder. Subsequently, the crest line splits, travels along each side, and then collides and shoots up behind the cylinder, as can be seen in the top figure. This kind of free-surface flow pattern around a vertical cylinder can also be observed in experiments, as reported in Miyata and Park [7]. The pressure field and time-limited streamlines along the symmetry plane corresponding to Plate 1 are also shown in Plate 2. In these cases, it can be seen that the fluid is not separated behind the cylinder.

4. CONCLUDING REMARKS

A finite difference simulation using a modified marker-and-cell (MAC) method was applied to investigate the characteristics of non-linear wave motions and their interactions with a stationary three-dimensional body inside a numerical wave tank (NWT). The Navier–Stokes (NS) equation was solved for two fluid layers by time marching and at every time step the Poisson equation was solved by an iterative procedure. The fully non-linear free-surface condition was satisfied by the density function method devised for two fluid layers. The incident waves were generated from the inflow boundary by prescribing a velocity profile resembling flexible flap-wavemaker motions, and the outflow waves were numerically dissipated inside an artificial damping zone located at the end of the tank. It was shown that the free-surface, inflow and open boundary treatments are robust.

The developed three-dimensional NS–MAC NWT was used to investigate the non-linear interaction of a vertical truncated circular cylinder with large-amplitude waves. The numerical method was verified through comparison with the experimental results of Mercier and Niedzwecki [12], an independently developed potential-based fully non-linear NWT, and the second-order diffraction computation. It was seen that the NWT simulations produced more reliable results for higher harmonic pressure, run-up, and forces compared with the second-order diffraction computation. In the numerical examples shown in this paper, the viscous NWT in general agreed well with the potential-based NWT, since the K–C number is small and the viscous effects play a relatively minor role.

The developed NS–MAC NWT is shown to be reliable and robust but it is still computationally very intensive. The typical CPU time for a five-period simulation of the vertical cylinder problem is about 40 h on a SGI Power Challenge 10000 XL based on the MIPS R10000. However, this kind of large CPU is not likely to be a serious problem in the future considering a rapid increase in computer power. The present scheme needs to include a proper turbulence modeling for large Reynolds number computations. Further development is also needed to simulate the non-linear motions of a floating body.

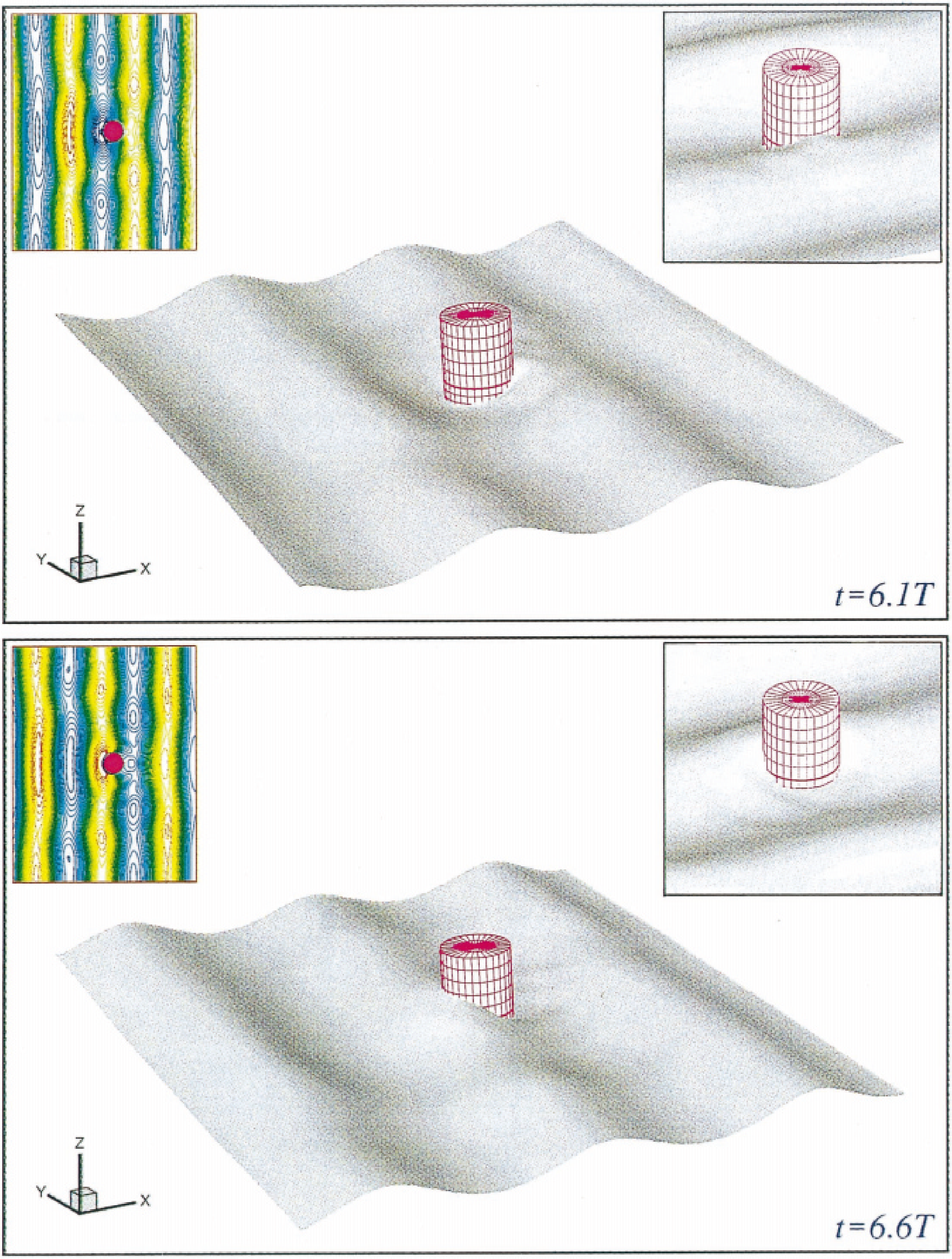

Plate 1. 3D and contour plots of diffracted wave field around a vertical cylinder.

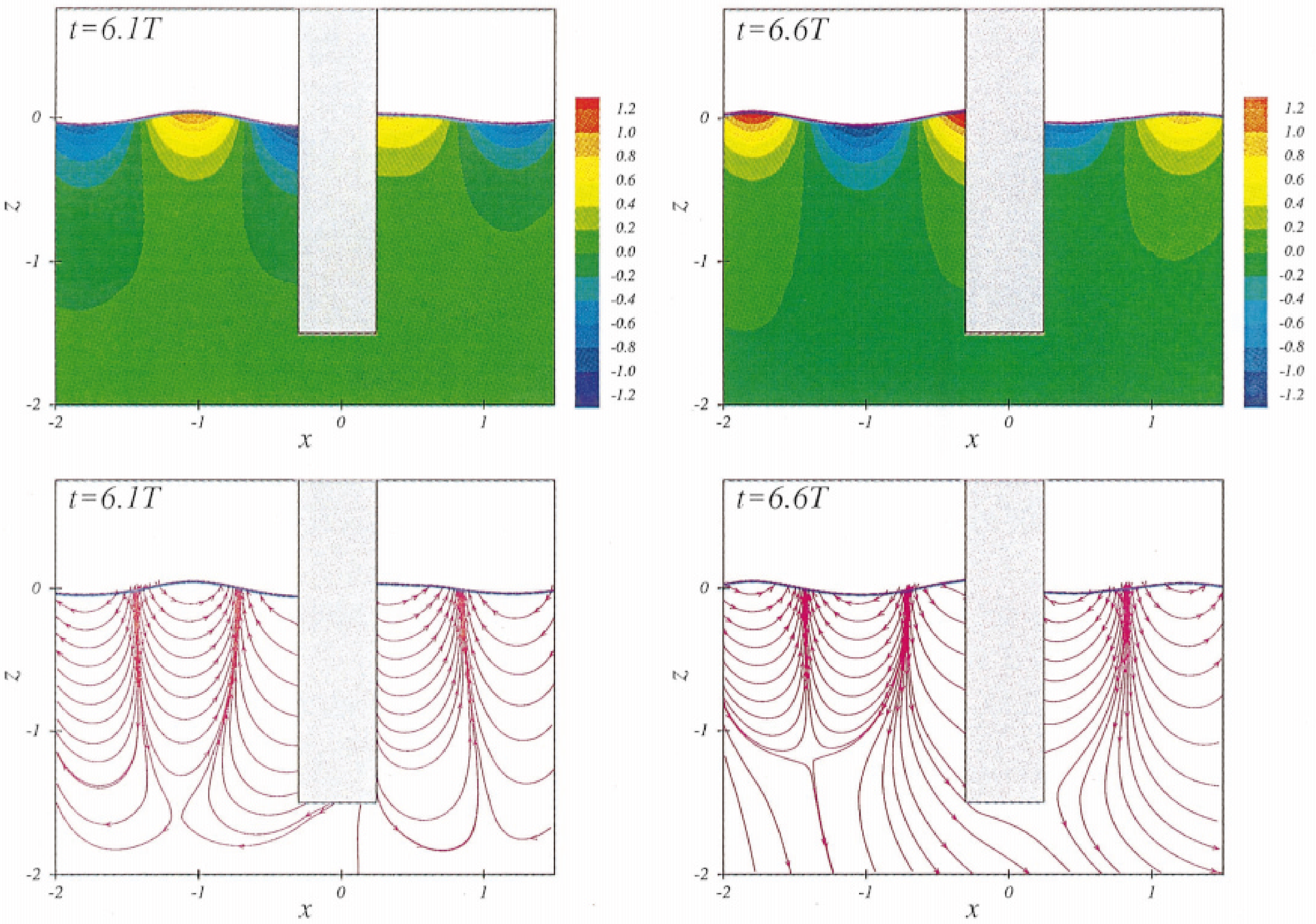

Plate 2. Time-limited streamlines and pressure field along the center plane.

REFERENCES

1. M.S. Longuet-Higgins and C.D. Cokelet, 'The deformation of steep surface waves on water, a numerical method of computation', *Proc. R Soc. Lond.*, **A350**, 1–26 (1976).
2. A. Clement, 'Coupling of two absorbing boundary conditions for 2D time domain simulations of free-surface gravity waves', *J. Comp. Phys.*, **126**, 139–151 (1996).
3. D.G. Dommermuth and D.K.P. Yue, 'Numerical simulations of non-linear axisymmetric flows with a free-surface', *J. Fluid Mech.*, **178**, 195–219 (1987).
4. R.F. Beck, 'Time domain computations for floating bodies', *J. Appl. Ocean Res.*, **16**, 267–282 (1994).
5. G.X. Wu and R. Eatock-Taylor, 'Finite element analysis of two-dimensional non-linear transient water waves', *J. Appl. Ocean Res.*, **16**, 363–372 (1994).
6. H.C. Chen, M. Chen, D.A. Davis and E.T. Huang, 'Time-domain simulation of a berthing DDG-51 ship by a domain decomposition approach', *Proc. ISOPE 1997*, Hawaii, 1997, pp. 58–587.
7. H. Miyata and J.-C. Park, 'Wave breaking simulation', in M. Rahman (ed.), *Advances in Fluid Mechanics, Potential Flow of Fluids*, Computational Mechanics Publications, UK, 1995, pp. 149–176.
8. J.-C. Park and H. Miyata, 'Numerical simulation of the non-linear free-surface flow caused by breaking waves, free-surface turbulence in Lake Tahoe', *ASME FED*, **181**, 155–168 (1994).
9. J.-C. Park, M. Zhu and H. Miyata, 'On the accuracy of numerical wave making techniques', *J. Soc. Naval Archit. Jpn.*, **173**, 35–44 (1993).
10. H. Miyata, H. Kajitani, M. Zhu and T. Kawano, 'Numerical study of some wave-breaking problems by a finite difference method', *J. Kansai Soc. Naval Archit. Jpn.*, **207**, 11–23 (1987).
11. H. Miyata and Y. Yamada, 'A finite difference method for 3D flows about bodies of complex geometry in rectangular co-ordinate systems', *Int. J. Numer. Methods Fluids*, **14**, 1261–1287 (1992).
12. R.S. Mercier and J.M. Niedzwecki, 'Experimental measurement of second-order diffraction by a truncated vertical cylinder in monochromatic waves', *Proc. 7th Int. Conf. Behavior of Offshore Structures*, **2**, 265–287 (1994).
13. B.D. Nichols and C.W. Hirt, 'Improved free-surface boundary conditions for numerical incompressible flow calculations', *J. Comput. Phys.*, **8**, 434–448 (1971).
14. K. Sawada and S. Takahashi, 'A numerical investigation on wing/nacelle interference of USB configuration', *AIAA Paper 87-0455*, 1987.
15. R.K.C. Chan and R.L. Street, 'A computer study of finite amplitude water waves', *J. Comput. Phys.*, **6**, 68–94 (1970).
16. M.S. Celebi and M.H. Kim 'Non-linear wave body interactions in a numerical wave tank', *Proc. 12th Int. Workshop on Water Waves and Floating Bodies*, France, 1997.
17. M.S. Celebi, M.H. Kim and R.F. Beck, 'Fully non-linear 3D numerical wave tank simulation', *J. Ship Res.*, **42**, 33–45 (1998).
18. M.H. Kim, M.S. Celebi and J.C. Park, 'Numerical wave tanks for non-linear wavebody interaction', *Int. Conf. Non-linear Design Aspects of Physical Model Tests*, College Station, TX, 1997.
19. M.H. Kim and D.K.P. Yue, 'The complete second-order diffraction solution for an axisymmetric body, part 1. Monochromatic incident waves', *J. Fluid Mech.*, **200**, 235–264 (1989).
20. C.H. Lee, J.N. Newman, M.H. Kim and D.K.P. Yue, 'The computation of second-order wave loads', *Proc. OMAE Conf.*, Stavanger, Norway, 1991.
21. M.S. Longuet-Higgins, 'A theory of the origin of microseisms', *Proc. R. Soc. Lond.*, **243**, 1–35 (1950).
22. J.N. Newman, 'Second-harmonic wave diffraction at large depths', *J. Fluid Mech.*, **213**, 59–70 (1990).